A Fast Hybrid Method for Scattering From a Large Object With Dihedral Effects Above a Large Rough Surface

Gildas Kubické and Christophe Bourlier, *Member, IEEE*

***Abstract*—A new hybrid numerical method is described for scattering from an electrically large perfectly-conducting object with dihedral effects above a very long one-dimensional rough surface (two-dimensional problem). Such a problem involves a large number of unknowns and cannot be solved easily with a conventional method of moments by using a direct LU inversion. Thus, to solve this issue, the Extended-PILE method is combined with the forward-backward spectral acceleration (FBSA) for the local interactions on the rough surface and with the second-order physical optics (PO2) approximation for the local interactions on the object. Classically objects under test do not present dihedral effects and in the high frequency domain the first-order PO (PO1) provides the main contribution. In opposite, in this paper since a cross is considered, the second-order inner reflections contribute significantly and the PO2 must be included. By assuming a Gaussian process with a Gaussian height spectrum, this new hybrid method, E-PILE+FBSA+PO2, is tested against the rigorous E-PILE+FBSA method (direct LU inversion on the object) as functions of the object inclination, the polarization and the incidence angle.**

***Index Terms*—Electromagnetic scattering by rough surfaces, hybrid algorithm, iterative methods, method of moments, object and rough surface, physical optics, radar cross section.**

I. Introduction

ELECTROMAGNETIC scattering from an object above a rough surface has attracted much interest during recent years. In order to solve this issue, some asymptotic and exact numerical models have been developed. Recent works have explored the three-dimensional (3D) combined object/rough surface scattering problem [1]–[5]. Nevertheless, since a brute force method of moments (MoM) can not be applied due to storage requirements, some simplifying assumptions must be made: (i) in [1], [2] only small problems are investigated from a fast rigorous numerical method; (ii) in [2]–[4] some assumptions are made on the coupling mechanisms from the four-path model; (iii) in [5] hybridization by using the asymptotic SPM (small perturbation method) is applied to calculate the local interactions on the rough surface, assumed to be slightly rough.

Thus, the 2D case is still investigated in order to compute the scattering from an object above a large one-dimensional rough surface like a multi-scale sea surface, for example. Although a 2D problem is considered, the brute force MoM can be applied only for small problems [6]. So, some fast rigorous numerical methods were proposed: (i) a parallelization of a rigorous method based on the MoM was proposed in [7]; (ii) in [8], a domain decomposition method with the finite-element method was applied; (iii) in [9], [10] an iterative scheme, the E-PILE (extended propagation-inside-layer expansion) method [11], was combined with the forward-backward spectral acceleration (FBSA) [12] to accelerate the computation of the local interactions on the rough surface; (iv) in [13] the fast multipole method is used to accelerate the computation of the local interactions on the object for a quite similar problem (the object is located on the rough surface).

Moreover, in order to decrease the computing requirements of the methods, simplifying assumptions and hybridization with asymptotic methods were proposed: (i) some assumption on the scattering mechanisms was made [14]; (ii) the MoM is combined with the physical optics (PO) for the local interactions on the rough surface [15], the MoM being applied for the local interactions on the object.

However, when the object is electrically large, the MoM (with direct LU inversion) can be unusable. In this paper, the effort is made on the use of PO for the calculation of the local interactions on the object in order to compute the scattering from a large object with dihedral effects above a large rough surface. Classically, objects under test do not present dihedral effects and in the high-frequency domain the first-order PO (PO1) provides the main contribution. In opposite, in this paper since a cross is considered, the second-order inner reflections mainly contribute to the radar cross section (RCS) and the second-order physical optics (PO2) approximation must be included. Due to the particular iterative scheme of the E-PILE method [9], [10], the FBSA is combined with the PO2 for the computation of the local interactions on the object. This new hybrid method, E-PILE+FBSA+PO2, permits to treat a large number of unknowns thanks to a storage requirement and computing time smaller than with a direct LU inversion.

The paper is organized as follows. The hybridization of E-PILE+FBSA with PO approximation is detailed in Section II. A brief summary of E-PILE+FBSA is addressed,

Manuscript received December 15, 2009; revised April 14, 2010; accepted June 26, 2010. Date of publication November 01, 2010; date of current version January 04, 2011. This work was supported by the French defence procurement agency DGA (Délégation Générale pour l'Armement) under REI Grant 2008.34.0041.

The authors are with Institut de Recherche en Electrotechnique et Electronique de Nantes Atlantique (IREENA) Laboratory, Fédération CNRS Atlanstic, Université de Nantes, 44306 Nantes Cedex 03, France (e-mail: gildas.kubicke@gmail.com).

Color versions of one or more of the figures in this paper are available online at http://ieeexplore.ieee.org.

Digital Object Identifier 10.1109/TAP.2010.2090470

then, as succinctly reported in [16], a plate above a rough surface is considered in order to combine E-PILE+FB-SA with PO1 (single reflection on the object), and, finally, a cross above a rough surface is considered for which E-PILE+FB-SA is combined with PO2 (single and double reflections on the object) for both TE and TM polarizations. Section III is devoted to numerical results. By assuming a Gaussian process with a Gaussian height spectrum, E-PILE+FBSA+PO2 is tested against the rigorous E-PILE+FBSA method (direct LU inversion on the object) as functions of the object inclination, the incidence angle and the polarization. Differences and complexity are also discussed. The last section gives concluding remarks.

II. Hybridization of E-PILE+FBSA With PO Approximation

A. The E-PILE Method Combined With FBSA

Let us consider an object located above a 1D rough surface as depicted in Fig. 1. The position vector on the object is $\boldsymbol{r_1} = (x_1, z_1)$ and the position vector on the rough surface is $\boldsymbol{r_2} = (x_2, z_2)$. The time convention $e^{-j\omega t}$ is assumed. From the integral equations on both surfaces, and by using the MoM with point matching and pulse basis functions, a linear system $\bar{\mathbf{Z}}\mathbf{X} = \mathbf{b} \Rightarrow \mathbf{X} = \bar{\mathbf{Z}}^{-1}\mathbf{b}$ is obtained, in which $\bar{\mathbf{Z}}$ is the impedance matrix of the scene $(\text{object} + \text{surface})$, $\mathbf{X}$ the vector containing the unknowns (the total field and its normal derivative) on both surfaces and $\mathbf{b}$ the incident field on the scene. If the scene is made up of a large object above a very long surface, the direct inversion of $\bar{\mathbf{Z}}$ cannot be done. One way to solve this difficult task is to apply the recently developed E-PILE method which is a rigorous numerical method for the scattering from two arbitrary scatterers [9] based on a Taylor expansion of the Schur complement. Indeed, one can show that the unknowns on the object surface $\mathbf{X}_1$ are obtained from

$$\mathbf{X}_1 = \sum_{p=0}^{P_{\text{PILE}}} \boldsymbol{X}_{\mathbf{1}}^{(\boldsymbol{p})} \tag{1}$$

in which

$$\begin{cases} \boldsymbol{X}_{\mathbf{1}}^{(\mathbf{0})} = \bar{\mathbf{Z}}_1^{-1}\left(\mathbf{b}_1 - \bar{\mathbf{Z}}_{21}\bar{\mathbf{Z}}_2^{-1}\mathbf{b}_2\right) & \text{for } p = 0 \\ \boldsymbol{X}_{\mathbf{1}}^{(\boldsymbol{p})} = \bar{\mathbf{M}}_{c,1}\boldsymbol{X}_{\mathbf{1}}^{(\boldsymbol{p-1})} & \text{for } p > 0 \end{cases} \tag{2}$$

in which $\bar{\mathbf{M}}_{c,1}$ is the characteristic matrix of the scene (the two scatterers) defined as $\bar{\mathbf{M}}_{c,1} = \bar{\mathbf{Z}}_1^{-1}\bar{\mathbf{Z}}_{21}\bar{\mathbf{Z}}_2^{-1}\bar{\mathbf{Z}}_{12}$ and $\mathbf{b}_1$ the incident field illuminating the object. $\bar{\mathbf{Z}}_1$ and $\bar{\mathbf{Z}}_2$ are the impedance matrices of scatterers 1 (object) and 2 (rough surface), respectively, whereas $\bar{\mathbf{Z}}_{12}$ and $\bar{\mathbf{Z}}_{21}$ can be interpreted as coupling matrices between the two scatterers. The mathematical expressions of these matrices, the interpretation of the E-PILE method, the acceleration with the FBSA method [12], the convergence, validity and complexity of E-PILE+FBSA method have been already detailed in [9], [11].

Since single and double reflections are the main contributions to the scattering from a cross, the next subsection focuses on the use of the first-order PO approximation in the E-PILE+FBSA algorithm.

B. The Plate Case: Single Reflection (PO1)

1) TM Case: For the TM polarization and for a PC (perfectly conducting) object in free space (without the rough surface), the total field on the object surface due to single reflection (SR) is given with PO1 approximation by

$$\psi(\boldsymbol{r_1}) = 2\psi_i(\boldsymbol{r_1}) \quad \forall \boldsymbol{r_1} \in S_i \tag{3}$$

in which S_i is the illuminated surface on the object excited by the incident field $\psi_i(\boldsymbol{r_1})$ and $\psi(\boldsymbol{r_1})$ is the total field on the object surface. If we consider two different sources which illuminate the object, one can write under PO1 approximation

$$\psi(\boldsymbol{r_1}) = 2(f(\boldsymbol{r_1})\psi_i(\boldsymbol{r_1}) + g(\boldsymbol{r_1})\psi_{21}(\boldsymbol{r_1})) = 2\psi_i'(\boldsymbol{r_1}) \tag{4}$$

in which $f(\boldsymbol{r_1})$ and $g(\boldsymbol{r_1})$ are two shadowing functions

$$\begin{cases} f(\boldsymbol{r_1}) = & 1 \quad \forall \boldsymbol{r_1} \in S_{\text{inc}} \\ f(\boldsymbol{r_1}) = & 0 \quad \text{otherwise} \end{cases} \tag{5}$$

and

$$\begin{cases} g(\boldsymbol{r_1}) = & 1 \quad \forall \boldsymbol{r_1} \in S_{i-21} \\ g(\boldsymbol{r_1}) = & 0 \quad \text{otherwise} \end{cases}. \tag{6}$$

S_{inc} is the excited surface with the incident field $\psi_i(\boldsymbol{r_1})$ and S_{i-21} is the illuminated surface on the object with the field $\psi_{21}(\boldsymbol{r_1})$. By sampling the object surface in N_1 elements, (4) can be converted into matrix

$$\boldsymbol{X}_{\mathbf{1_{PO1}}} = 2(\bar{\boldsymbol{F}}\boldsymbol{b_1} + \bar{\boldsymbol{G}}\boldsymbol{b_{21}}) = 2\boldsymbol{u'} \tag{7}$$

in which $\boldsymbol{X}_{\mathbf{1_{PO1}}}$ is the unknown vector containing only the total field on the object $\psi(\boldsymbol{r}_{\mathbf{1}_n})$ sampled on the surface ($n \in [1; N_1]$ and $\boldsymbol{r}_{\mathbf{1}_n} \in S_1$). $\bar{\boldsymbol{F}}$ and $\bar{\boldsymbol{G}}$ are identity matrices in which some elements are set to zero due to PO1 shadowing (sampling of the shadowing functions $f(\boldsymbol{r_1})$ and $g(\boldsymbol{r_1})$)

$$\begin{cases} (\bar{\boldsymbol{F}})_{nn} = & 1 \text{ if } \boldsymbol{r}_{\mathbf{1}_n} \in S_{\text{inc}} \\ (\bar{\boldsymbol{F}})_{mn} = & 0 \text{ otherwise} \end{cases} \tag{8}$$

and

$$\begin{cases} (\bar{\boldsymbol{G}})_{nn} = & 1 \text{ if } \boldsymbol{r}_{\mathbf{1}_n} \in S_{i-21} \\ (\bar{\boldsymbol{G}})_{mn} = & 0 \text{ otherwise} \end{cases}. \tag{9}$$

By considering the 0th order $(P_{\text{PILE}} = 0)$ of E-PILE+FBSA, (7) is quite similar to (2). Indeed, the unknowns $\boldsymbol{X}_{\mathbf{1}}^{(\mathbf{0})}$ on the object can be expressed as

$$\boldsymbol{X}_{\mathbf{1}}^{(\mathbf{0})} = \bar{\boldsymbol{Z}}_{\mathbf{1}}^{-1}\boldsymbol{u} \tag{10}$$

in which $\boldsymbol{u}$ can be seen as an incident field on the object:

$$\boldsymbol{u} = \boldsymbol{b_1} - \bar{\boldsymbol{Z}}_{\mathbf{21}}\bar{\boldsymbol{Z}}_{\mathbf{2}}^{-1}\boldsymbol{b_2}. \tag{11}$$

Moreover, in the E-PILE algorithm, one can split up the excitation into two sources [9]: one due to direct illumination of the incident field $\boldsymbol{b_1}$ and the other one due to coupling (multiple interactions) with the rough surface $\bar{\boldsymbol{Z}}_{21}\boldsymbol{v}$ where $\boldsymbol{v}$ is a field on the rough surface (see (11)). Thus, the excited surfaces on the object are not the same according to the considered source. Indeed, as we can see in Fig. 1, the incident field illuminates the top side of the plate whereas the field scattered from the rough surface toward the object illuminates the bottom side of the plate.

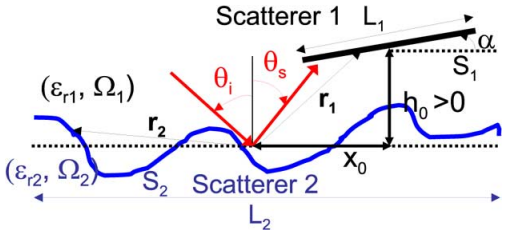

Fig. 1. Description of the problem: a perfectly conducting plate is located above a rough surface. The media $\{\Omega_1, \Omega_2\}$ of permittivities $\{\epsilon_{r1}, \epsilon_{r2}\}$ are assumed to be homogeneous, and the surfaces are invariant along the direction normal to the figure (2D problem).

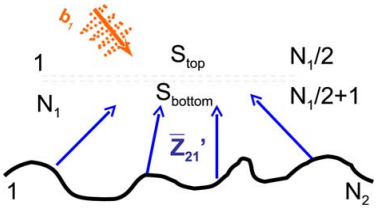

Fig. 2. Illustration of the propagation paths (according to PO1) for an horizontal plate above a rough surface.

Thus, from (10), (11) and (7), we have

$$\boldsymbol{X_1}^{(0)} = 2\left[\boldsymbol{b_1'} - \bar{\boldsymbol{Z}}'_{\boldsymbol{21}}\bar{\mathbf{Z}}_2^{-1}\mathbf{b}_2\right] = 2\boldsymbol{u'} \tag{12}$$

in which $\boldsymbol{b_1'} = \bar{\boldsymbol{F}}\boldsymbol{b_1}, \bar{\boldsymbol{Z}}'_{\boldsymbol{21}} = \bar{\boldsymbol{G}}\bar{\mathbf{Z}}_{21}$, Thus, the inversion of $\bar{\boldsymbol{Z}}_{\boldsymbol{1}}$ becomes analytic and straightforward. The shadowing is taken into account in the source vector $\boldsymbol{u'}$. Moreover, the matrix-vector product $\bar{\boldsymbol{Z}}_{\boldsymbol{1}}^{-1}\boldsymbol{u}$ becomes a scalar-vector product $2\boldsymbol{u'}$.

At the order P_{PILE} in the E-PILE process, since $\bar{\boldsymbol{M}}_{\boldsymbol{c,1}}$ realizes a back and forth between the two scatterers [9] (which rigorously takes into account coupling effect), the total field $\boldsymbol{X_1}$ on the object is expressed from (1) in which $\boldsymbol{X_1}^{(0)}$ is given by (12) and the pth order is given by

$$\boldsymbol{X_1^{(p)}} = \bar{\boldsymbol{M}}'_{\boldsymbol{c,1}}\boldsymbol{X_1^{(p-1)}} \tag{13}$$

in which $\bar{\boldsymbol{M}}'_{\boldsymbol{c,1}} = 2\bar{\boldsymbol{Z}}'_{\boldsymbol{21}}\bar{\mathbf{Z}}_2^{-1}\bar{\mathbf{Z}}_{12}$.

Now, the difficulty is to define the illuminated surfaces S_{inc} and S_{i-21} which are necessary to obtain the modified vector $\boldsymbol{b_1'}$ and coupling matrix $\bar{\boldsymbol{Z}}'_{\boldsymbol{21}}$ (see (8) and (9)). Indeed, the incident field illuminates the top side of the plate (surface S_{top}: samples numbered $1 \ldots N_1/2$) but the field scattered from the rough surface toward the object can illuminate both the top side and the bottom side of the plate: it depends on the plate inclination α. This PO1 shadowing, which defines if the element "n" of the object belongs to the excited face (directly excited) or to the shadowed surface (not directly excited) of the object, can be computed from geometrical considerations and taken into account by means of booleans: $(\boldsymbol{b_1'})_n = (\boldsymbol{b_1})_n(\beta_1)_n$ and $(\bar{\boldsymbol{Z}}'_{\boldsymbol{21}})_{mn} = (\bar{\boldsymbol{Z}}_{\boldsymbol{21}})_{mn}(\beta_{21})_{mn}$ in which

$$(\beta_1)_n = \frac{1+\mathrm{sign}[v_n\gamma_{1_n}\sin(\theta_i)+v_n\cos(\theta_i)]}{2} \tag{14}$$

$$(\beta_{21})_{mn} = \frac{1+\mathrm{sign}[(x_{1_m}-x_{2_n})v_m\gamma_{1_m}-(z_{1_m}-z_{2_n})v_m]}{2} \tag{15}$$

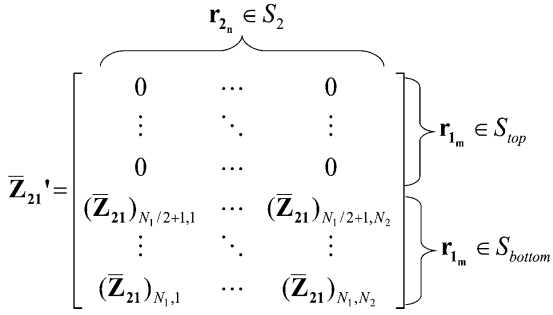

Fig. 3. Resulting modified coupling matrix for an horizontal plate above a rough surface.

where v_n defines the orientation of the plate normal vector ($v_n = +1$ for $n = 1, \ldots, N_1/2$ and $v_n = -1$ for $n = N_1/2+1, \ldots, N_1$), γ_{1_n} is the slope of the surface object at the point $\boldsymbol{r_{1_n}}$. Let us consider an horizontal plate above a rough surface, as depicted in Fig. 2, to illustrate the modified vector $\boldsymbol{b_1'}$ and coupling matrix $\bar{\boldsymbol{Z}}'_{\boldsymbol{21}}$. By using (14), $\boldsymbol{b_1'}$ is given by

$$\boldsymbol{b_1}' = \begin{bmatrix} \psi_i(\boldsymbol{r_{1_1}}) \\ \vdots \\ \psi_i(\boldsymbol{r_{1_{N_1/2}}}) \\ 0 \\ \vdots \\ 0 \end{bmatrix} \begin{matrix} \} \ \boldsymbol{r_n} \in S_{\mathrm{top}} \\ \\ \} \ \boldsymbol{r_n} \in S_{\mathrm{bottom}} \end{matrix} \tag{16}$$

and by using (15), $\bar{\boldsymbol{Z}}_{\boldsymbol{21}}$ is modified as depicted in Fig. 3.

In conclusion, the impedance matrix $\bar{\boldsymbol{Z}}_{\boldsymbol{1}}$ is not stored ($\mathcal{O}(N_1^2) \rightarrow 1$), its inversion is analytic (not computed: $\mathcal{O}(N_1^3) \rightarrow 1$) and the computing time is also reduced for the matrix-vector product $\bar{\boldsymbol{Z}}_{\boldsymbol{1}}^{-1}\boldsymbol{v}$ (for any incident field vector $\boldsymbol{v}$); PO1 shadowing effects being geometrically taken into account during the incident vector and coupling matrix fillings.

2) TE Case: For TE polarization, and for a PC object, the Dirichlet boundary condition implies $\psi(\boldsymbol{r}) = 0$, thus, $\boldsymbol{X_1}$ is the unknown vector containing only the normal derivative of the total field on the object $\partial\psi_i(\boldsymbol{r_n})/\partial n_1$ sampled on the surface. And with PO1, for an object in free space, we have

$$\frac{\partial\psi(\boldsymbol{r})}{\partial n_1} = 2\frac{\partial\psi_i(\boldsymbol{r})}{\partial n_1} \quad \forall \boldsymbol{r} \in S_i \tag{17}$$

and for two sources

$$\frac{\partial\psi(\boldsymbol{r})}{\partial n_1} = 2\left[f(\boldsymbol{r})\frac{\partial\psi_i(\boldsymbol{r})}{\partial n_1} + g(\boldsymbol{r})\frac{\partial\psi_{21}(\boldsymbol{r})}{\partial n_1}\right] = 2\frac{\partial\psi'_i}{\partial n_1}. \tag{18}$$

Using the same way as for the TM case, the normal derivative of the total field $\boldsymbol{X_1}$ on the object is expressed from (1) in which $\boldsymbol{X_1}^{(0)}$ is given by (12) and the pth order is given by (13) in which $\bar{\boldsymbol{M}}'_{\boldsymbol{c,1}} = 2\bar{\boldsymbol{Z}}'_{\boldsymbol{21}}\bar{\mathbf{Z}}_2^{-1}\bar{\mathbf{Z}}_{12}$ with $(\boldsymbol{b_1'})_n = (\partial\bullet)/(\partial n_1)(\boldsymbol{b_1})_n(\beta_1)_n$ and $(\bar{\boldsymbol{Z}}'_{\boldsymbol{21}})_{mn} = (\partial\bullet)/(\partial n_1)(\bar{\boldsymbol{Z}}_{\boldsymbol{21}})_{mn}(\beta_{21})_{mn}$; $(\partial\bullet)/(\partial n_1)$ is the normal derivative which operates on the coordinates (x_1, z_1) of the elements of $\boldsymbol{b_1}$ and $\bar{\boldsymbol{Z}}_{\boldsymbol{21}}$. Once again, the impedance matrix $\bar{\boldsymbol{Z}}_{\boldsymbol{1}}$ is not stored, its inversion is analytic (not computed) and the computing time is also reduced for the matrix-vector product $\bar{\boldsymbol{Z}}_{\boldsymbol{1}}^{-1}\boldsymbol{v}$ (for any incident field vector $\boldsymbol{v}$). The calculus of

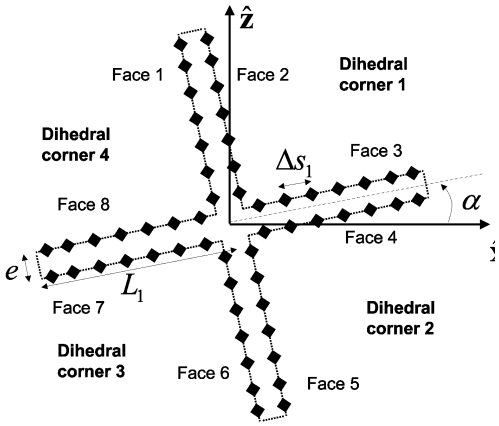

Fig. 4. Description of the perfectly conducting cross constituted by 4 dihedral corners (8 faces). The surface is invariant along the direction normal to the figure (2D problem).

$\boldsymbol{b_1'}$ is obtained from the normal derivative of the tapered incident wave (the Thorsos wave is used to avoid edge effects [17]) [18]. The detailed calculus of $\bar{\boldsymbol{Z}}_{\boldsymbol{21}}'$ for TE polarization is given in Appendix A.

C. The Cross Case: Single and Double Reflections (PO2)

Now, let us consider an electrically large PC object constituted by dihedral corners. Thus, second-inner reflections must be included in the model since double reflections (DR) occur due to dihedral effects. To investigate this, a PC cross, constituted by 4 PC plates (8 faces) which create 4 dihedral corners as depicted in Fig. 4, is located above a 1D rough surface.

1) TE Case: Since in dihedral corners the SR and DR mainly contribute to the radar cross section (RCS), the unknowns on the cross are split into two components: the SR contributions and the DR ones

$$\boldsymbol{X_1} = \boldsymbol{X_1^{SR}} + \boldsymbol{X_1^{DR}} \tag{19}$$

in which $\boldsymbol{X_1^{SR}}$ is computed from (12) and (13) in which the booleans $(\beta_1)_n$ and $(\beta_{21})_{mn}$ are different since there are additional blockage effects. They are given from geometrical projections of the cross vertices in each dihedral corner as a function of the exciting field vector (incident field vector $\boldsymbol{k_i}$ or scattered field vector from the rough surface $\boldsymbol{k_{21}}$).

$\boldsymbol{X_1^{DR}}$ is computed by propagating the surface currents from a face of a dihedral corner to the opposite face. Under PO approximation, there are only 8 DR (PO2 shadowing): $(f_2 \rightsquigarrow f_3)$ and $(f_3 \rightsquigarrow f_2), (f_4 \rightsquigarrow f_5)$ and $(f_5 \rightsquigarrow f_4), (f_6 \rightsquigarrow f_7)$ and $(f_7 \rightsquigarrow f_6), (f_8 \rightsquigarrow f_1)$ and $(f_1 \rightsquigarrow f_8)$ (f_i stands for the ith face—see Fig. 4 for the face numbers), thus $\boldsymbol{X_1^{DR}}$ is computed from $\boldsymbol{X_1^{SR}}$ by

$$\boldsymbol{X_1^{DR}} = \bar{\boldsymbol{Z}}_{\boldsymbol{1}}^{-1} \bar{\boldsymbol{C}}_{\mathbf{DR}} \boldsymbol{X_1^{SR}} \tag{20}$$

in which $\bar{\boldsymbol{Z}}_{\boldsymbol{1}}^{-1}$ computes the local interactions on the cross due to an exciting field. Thus, according to PO approximation we have

$$\boldsymbol{X_1^{DR}} = 2\bar{\boldsymbol{C}}_{\mathbf{DR}} \boldsymbol{X_1^{SR}}. \tag{21}$$

$$\bar{\mathbf{C}}_{\mathrm{DR}} = \begin{bmatrix} \bar{\mathbf{0}} & \bar{\mathbf{0}} & \bar{\mathbf{0}} & \bar{\mathbf{0}} & \bar{\mathbf{0}} & \bar{\mathbf{0}} & \bar{\mathbf{0}} & \bar{\mathbf{C}}_{\mathbf{f_8 \to f_1}} \\ \bar{\mathbf{0}} & \bar{\mathbf{0}} & \bar{\mathbf{C}}_{\mathbf{f_3 \to f_2}} & \bar{\mathbf{0}} & \bar{\mathbf{0}} & \bar{\mathbf{0}} & \bar{\mathbf{0}} & \bar{\mathbf{0}} \\ \bar{\mathbf{0}} & \bar{\mathbf{C}}_{\mathbf{f_2 \to f_3}} & \bar{\mathbf{0}} & \bar{\mathbf{0}} & \bar{\mathbf{0}} & \bar{\mathbf{0}} & \bar{\mathbf{0}} & \bar{\mathbf{0}} \\ \bar{\mathbf{0}} & \bar{\mathbf{0}} & \bar{\mathbf{0}} & \bar{\mathbf{0}} & \bar{\mathbf{C}}_{\mathbf{f_5 \to f_4}} & \bar{\mathbf{0}} & \bar{\mathbf{0}} & \bar{\mathbf{0}} \\ \bar{\mathbf{0}} & \bar{\mathbf{0}} & \bar{\mathbf{0}} & \bar{\mathbf{C}}_{\mathbf{f_4 \to f_5}} & \bar{\mathbf{0}} & \bar{\mathbf{0}} & \bar{\mathbf{0}} & \bar{\mathbf{0}} \\ \bar{\mathbf{0}} & \bar{\mathbf{0}} & \bar{\mathbf{0}} & \bar{\mathbf{0}} & \bar{\mathbf{0}} & \bar{\mathbf{0}} & \bar{\mathbf{C}}_{\mathbf{f_7 \to f_6}} & \bar{\mathbf{0}} \\ \bar{\mathbf{0}} & \bar{\mathbf{0}} & \bar{\mathbf{0}} & \bar{\mathbf{0}} & \bar{\mathbf{0}} & \bar{\mathbf{C}}_{\mathbf{f_6 \to f_7}} & \bar{\mathbf{0}} & \bar{\mathbf{0}} \\ \bar{\mathbf{C}}_{\mathbf{f_1 \to f_8}} & \bar{\mathbf{0}} & \bar{\mathbf{0}} & \bar{\mathbf{0}} & \bar{\mathbf{0}} & \bar{\mathbf{0}} & \bar{\mathbf{0}} & \bar{\mathbf{0}} \end{bmatrix}$$

Fig. 5. Illustration of the coupling matrix $\bar{\boldsymbol{C}}_{\mathbf{DR}}$ for the double reflections of the cross.

The propagation of the surface currents between faces is taken into account by the coupling matrix $\bar{\boldsymbol{C}}_{\mathbf{DR}}$ in which PO2 shadowing are considered. This matrix is illustrated in Fig. 5 in which $\bar{\mathbf{0}}$ is an empty matrix of size $n_i \times n_j$ with n_i and n_j the sample number on the ith and jth faces.

$\bar{\boldsymbol{C}}_{\boldsymbol{f}i \rightsquigarrow \boldsymbol{f}j}$ is given by

$$\bar{\boldsymbol{C}}_{\boldsymbol{f}i \rightsquigarrow \boldsymbol{f}j} = \begin{bmatrix} (\bar{\boldsymbol{C}}_{\mathbf{DR}})_{n_i^{(1)}, n_j^{(1)}} & \cdots & (\bar{\boldsymbol{C}}_{\mathbf{DR}})_{n_i^{(1)}, n_j^{(N_f)}} \\ \vdots & \ddots & \vdots \\ (\bar{\boldsymbol{C}}_{\mathbf{DR}})_{n_i^{(N_f)}, n_j^{(1)}} & \cdots & (\bar{\boldsymbol{C}}_{\mathbf{DR}})_{n_i^{(N_f)}, n_j^{(N_f)}} \end{bmatrix} \tag{22}$$

where $n_i^{(1)}, n_j^{(1)}$ are the local indexes of the first point of ith and jth faces, respectively and $n_i^{(N_f)}$ and $n_j^{(N_f)}$ are last ones. The elements of the sub-matrices $\bar{\boldsymbol{C}}_{\boldsymbol{f_i \rightsquigarrow f_j}}$ are given in Appendix B.

From (19) and (21), we have

$$\boldsymbol{X_1} = \left(\bar{\boldsymbol{I}} + 2\bar{\boldsymbol{C}}_{\mathbf{DR}}\right) \boldsymbol{X_1^{SR}}. \tag{23}$$

Since $\boldsymbol{X_1^{SR}}$ is given at the 0th order of E-PILE+FBSA from (12), we have

$$\boldsymbol{X_1}^{(0)} = (\bar{\boldsymbol{I}} + 2\bar{\boldsymbol{C}}_{\mathbf{DR}}) 2 \left[\boldsymbol{b_1'} - \bar{\boldsymbol{Z}}_{\boldsymbol{21}}' \bar{\mathbf{Z}}_2^{-1} \mathbf{b}_2\right] \tag{24}$$

and, from (10), (11), one can identify the inverted impedance matrix of the cross under PO2 $(\mathrm{SR} + \mathrm{DR})$ approximation

$$\bar{\boldsymbol{Z}}_{\boldsymbol{1}}^{-1} = 2\left(\bar{\boldsymbol{I}} + 2\bar{\boldsymbol{C}}_{\mathbf{DR}}\right). \tag{25}$$

Finally, at the order P_{PILE} in the E-PILE process, the total field $\boldsymbol{X_1}$ on the cross is expressed from (1) in which $\boldsymbol{X_1}^{(0)}$ is given by (24) and the pth order is given by

$$\boldsymbol{X_1^{(p)}} = \bar{\boldsymbol{M}}_{\boldsymbol{c,1}}' \boldsymbol{X_1^{(p-1)}} \tag{26}$$

in which $\bar{\boldsymbol{M}}_{\boldsymbol{c,1}}' = (\bar{\boldsymbol{I}} + 2\bar{\boldsymbol{C}}_{\mathbf{DR}}) 2 \bar{\boldsymbol{Z}}_{\boldsymbol{21}}' \bar{\mathbf{Z}}_2^{-1} \bar{\mathbf{Z}}_{12}$.

In conclusion, the inversion of the impedance matrix $\bar{\boldsymbol{Z}}_{\boldsymbol{1}}$ is analytic (not computed: $\mathcal{O}(N_1^3) \rightarrow 1$). But, in contrary to the plate case, the impedance matrix $\bar{\boldsymbol{Z}}_{\boldsymbol{1}}^{-1}$ is not a scalar but a sparse matrix: the non-zero elements of $\bar{\boldsymbol{C}}_{\mathbf{DR}}$ have to be stored. The storage requirement for the local interactions on the object from a rigorous approach (direct LU inversion) is divided by 8 with PO2.

III. Numerical Results

A. Validity

The hybrid method is tested for several configurations. For all simulations presented here, the rough surface is perfectly-conducting and it obeys a Gaussian process with a Gaussian height spectrum with root mean square height $\sigma_z = 0.5\lambda_0$, correlation length $L_c = 2\lambda_0$, surface length $L_2 = 1000\lambda_0$, sampling step on the rough surface $\Delta_{x_2} = \lambda_0/10$ ($N_2 = 10000$ samples on the rough surface); λ_0 being the wavelength in the vacuum. A perfectly-conducting surface provides a higher coupling effect between the object and the surface which permits us to better exhibit limitations of the hybrid method. Since the Method of Moments (with a direct LU inversion) cannot be used with a standard computer with a high number of unknowns, the benchmark method is the E-PILE+FBSA+LU method. Thus, with the benchmark method, a direct LU inversion is used for the computation of local interactions on the object whereas with the hybrid method, PO is applied. Parameters of E-PILE+FBSA are $P_{\mathrm{FB}} = \{5, 2\}$ (order of the iterative scheme involved in the Forward-Backward algorithm) for $\{\mathrm{TE}, \mathrm{TM}\}$ polarization, respectively, $x_{d0} = 3L_c$ (strong interaction length for the Spectral Acceleration), and $P_{\mathrm{PILE}} = 3$ (order of the iterative scheme involved in the E-PILE algorithm). This parametrization was already studied in details in [9], [10], [19] and it was shown that a good convergence is obtained with these values whatever the object shape.

1) The Plate Case: The plate has a length $L_1 = 20\lambda_0$ and it is described by $N_1 = 400$ samples (200 samples for each face). The thickness of the plate is $e = \lambda_0/15$ smaller than the sampling step in order to simulate a zero-thickness plate (this assumption was validated from several simulations). The center of the plate is located at $(x_0 = -h_0 \tan(\theta_i), h_0 = 15\lambda)$ in such a way that it is centered on the tapered incident wave.

The total field $|\psi_1|$ on the plate surface computed from the hybrid method is compared with that obtained from the benchmark method versus the samples on the object in Fig. 6. The incidence angle is $\theta_i = 30°$, the plate orientation is $\alpha = 0°$, and TM polarization is considered.

As said before, with $\alpha = 0°$ and under PO approximation, the field scattered from the rough surface illuminates only the face 2 (bottom side), whereas the incident wave illuminates only the face 1 (top side). Consequently, currents are constant on face 1 (equals twice the incident field) and coupling mechanisms with the rough surface imply a non-null current on face 2. The edge effects are neglected under PO approximation: the variation of the current is not predicted and its concentration on the right edge (for $N_1 = 200$) is under estimated with the hybrid method. Nevertheless, the currents are in good agreement on face 2 with that of the benchmark method.

In Fig. 7, the bistatic normalized radar cross-section obtained from the hybrid method is compared with that obtained from the benchmark method versus the scattering angle θ_s, with same parameters as in Fig. 6. In addition, the relative residual error (RRE) of the hybrid method is reported in the legend. The RRE is given by $\mathrm{RRE} = \mathrm{norm}(\boldsymbol{\sigma}_{\mathrm{hyb}} - \boldsymbol{\sigma}_{\mathrm{ref}})/\mathrm{norm}(\boldsymbol{\sigma}_{\mathrm{ref}})$ in which "norm" corresponds to the Euclidean norm of a vector, $\boldsymbol{\sigma}_{\mathrm{hyb}}$ and $\boldsymbol{\sigma}_{\mathrm{ref}}$ are the vectors which contain the NRCS versus the scattering angle ($\theta_s \in]-90; 90[$) computed from the hybrid method and the benchmark one, respectively.

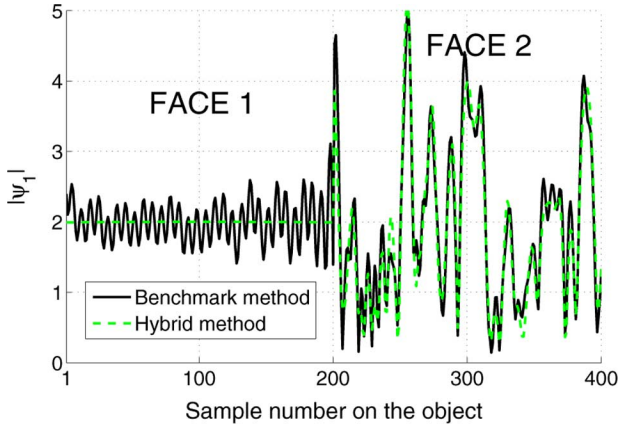

Fig. 6. Comparison of the total field $|\psi_1|$ on the plate surface computed from the hybrid method (E-PILE+FBSA+PO1) with that obtained from the benchmark method (E-PILE+FBSA+LU) versus the samples on the object. The parameters are $L_2 = 1000\lambda, \sigma_z = 0.5\lambda, L_c = 2\lambda, L_1 = 20\lambda, (x_0 = -h_0 \tan(\theta_i), h_0 = 15\lambda), \alpha = 0°, \theta_i = 30°$, TM polarization.

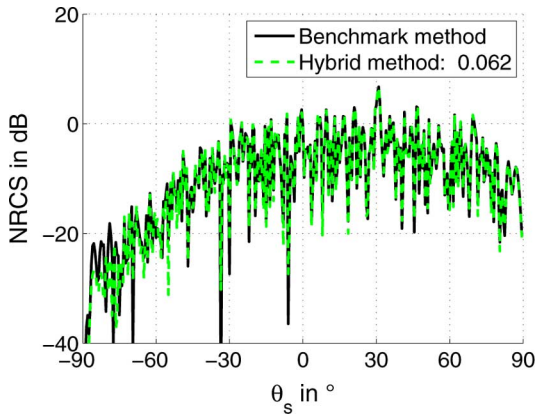

Fig. 7. Comparison of the normalized radar cross-section of a plate above a rough surface computed from the hybrid method with that obtained from the benchmark method versus the scattering angle. Same parameters as in Fig. 6. In addition, the RRE is reported in the legend.

Same comparison as in Fig. 7, but for the TE polarization, is plotted in Fig. 8.

From Figs. 7 and 8, a very good agreement is observed between the hybrid method and the benchmark one. Indeed, the RRE is mainly due to differences which appear for $\theta_s < -70°$. Same conclusion and similar RRE are obtained from other simulations (with other values of θ_i and α). These differences at grazing observation angles can be due to the edge diffraction that is neglected with the hybrid method.

2) The Cross Case: The hybrid method is now tested for a cross above the rough surface. Each plate of the cross has a length $L_1 = 10\lambda_0$ and a thickness $e = \lambda_0/15$ (smaller than the sampling step) and the cross is described by $N_1 = 800$ samples (100 samples for each face). The center of the cross is located at $(x_0 = -h_0 \tan(\theta_i), h_0 = 15\lambda)$.

In Fig. 9, the bistatic normalized radar cross-section of the cross above a rough surface computed from the hybrid method is compared with that obtained from the benchmark method versus

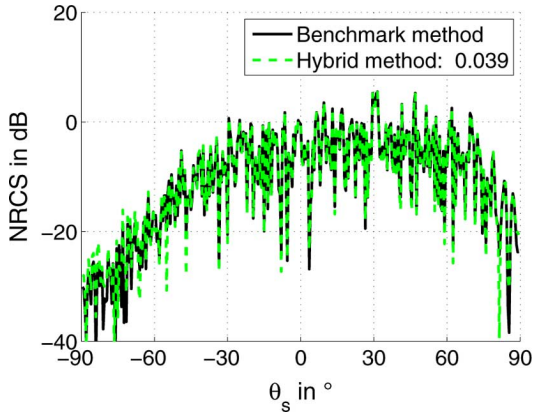

Fig. 8. Same as in Fig. 7 but TE polarization is considered.

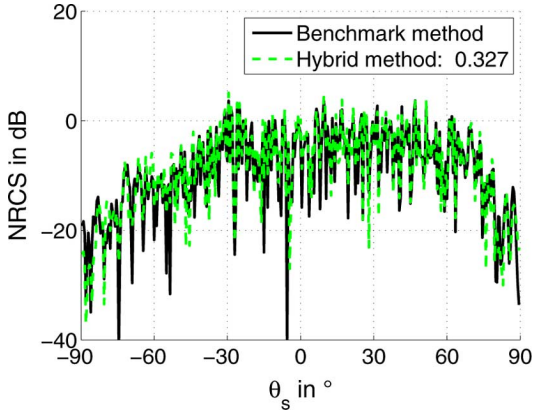

Fig. 9. Comparison of the normalized radar cross-section of a cross above a rough surface computed from the hybrid method with that obtained from the benchmark method versus the scattering angle. The parameters are $L_2 = 1000\lambda, \sigma_z = 0.5\lambda, L_c = 2\lambda, L_1 = 10\lambda, (x_0 = -h_0 \tan(\theta_i), h_0 = 15\lambda)$, $\alpha = 0°, \theta_i = 30°$, TE polarization. In addition, the RRE is reported in the legend.

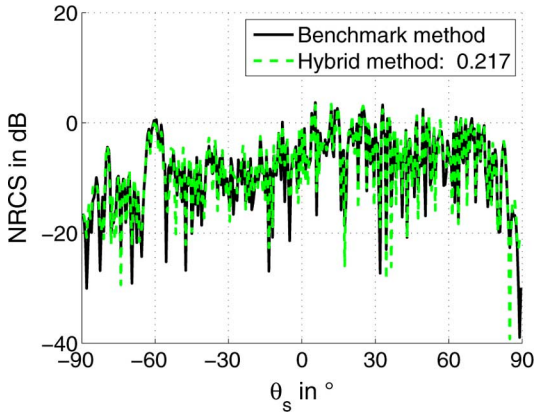

Fig. 10. Same as in Fig. 9 but with $\theta_i = 60°$.

the scattering angle θ_s. The incidence angle is $\theta_i = 30°$, the plate orientation is $\alpha = 0°$, and TE polarization is considered.

Same comparison as in Fig. 9 but with $\theta_i = 60°$, is plotted in Fig. 10.

From Figs. 9–10, a very good agreement is observed between the hybrid method and the benchmark one on the NRCS results.

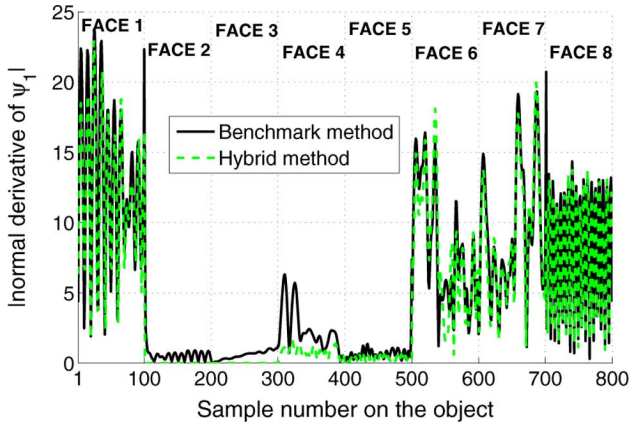

Fig. 11. Comparison of the normal derivative of the total field $|\partial\psi_1/\partial n_1|$ on the cross surface computed from the hybrid method (E-PILE+FBSA+PO2) with that obtained from the benchmark method (E-PILE+FBSA+LU) versus the samples on the cross. Same scene as in Fig. 10 is considered.

The RRE is higher for the cross case than for the plate case. This is mainly due to very localized discrepancies at particular scattering angles θ_s for which there is a strong attenuation of NRCS. Nevertheless, the NRCS is very well evaluated with the hybrid method. Same conclusions were made with other simulations. As for the plate case, some differences appear at grazing observation angles (for $\theta_s < -70°$), which can be due to the edge diffraction that is neglected with the hybrid method.

The normal derivative of the total field $|\partial\psi_1/\partial n_1|$ on the cross surface, for the same scene as in Fig. 10, is plotted in Fig. 11. By considering the cross geometry (see Fig. 4), with $\alpha = 0°$ and under PO approximation, the field scattered from the rough surface illuminates faces 4 to 7 whereas the incident wave illuminates faces 8 and 1 only. The face 3 is not excited by the incident wave due to the shadowing by the face 1. Consequently, a null current is set on faces 2 and 3. Moreover, double reflections between faces 1 and 8 are created by the incident field. This can be observed from Fig. 6.

As one can see, there is a strong coupling between the rough surface and the faces 6 and 7 of the cross which provides double reflections. As for the plate case, the concentration of the currents on some edges (for $N_1 = 1, N_1 = 100$ and $N_1 = 700$ here) is under estimated with the hybrid method. Nevertheless, by means of PO2, currents obtained from the hybrid method are in good agreement with that obtained from the benchmark method.

B. Complexity

The complexity (number of multiplications) of both hybrid and benchmark method is given by

$$T_{\text{CPU}} = T_1 + 2\{T_{11} + T_{12} + T_2\} + 2P_{\text{PILE}}\{T_{11} + 2T_{12} + T_2\} \quad (27)$$

in which

- T_{12} is the complexity of the matrix-vector product for a coupling step (object toward surface or surface toward object);

TABLE I
COMPLEXITY OF E-PILE+FBSA, E-PILE+FBSA+PO1 (PLATE CASE) AND E-PILE+FBSA+PO2 (CROSS CASE) FOR T_1, T_{11} AND T_{12}

Configuration \ Complexity	T_1	T_{11}	T_{12}
E-PILE+FBSA	$N_1^3/3$	N_1^2	N_1N_2
E-PILE+FBSA+PO1	0	1	$3N_1N_2/4$
E-PILE+FBSA+PO2	0	$N_1^2/8$	$3N_1N_2/4$

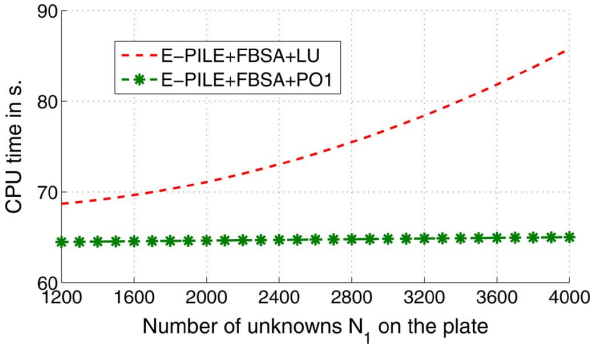

Fig. 12. Comparison of computing time of the hybrid and rigorous methods versus the number of unknowns on the plate for a plate above a rough surface. Same parameters as in Fig. 7.

- T_{11} is the complexity of the matrix-vector product for the local interactions on the object;
- T_1 is the complexity of the matrix inversion for the local interactions on the object;
- T_2 is the complexity of both the matrix inversion and the matrix-vector product for the local interactions on the rough surface.

The complexity of the rigorous method (E-PILE+FBSA+LU) is given in details in [9]. For both hybrid (E-PILE+FBSA+PO) and rigorous methods, T_2 depends on the complexity of the FBSA method: $T_2 = \mathcal{O}(N_2)$. The complexities of T_1, T_{11} and T_{12} from the benchmark and hybrid methods are compared in Table I. For example, $T_{12} = N_1N_2$ for the rigorous method and it is reduced to $T_{12} = 3N_1N_2/4$ for the hybrid method by taking advantage of the sparse coupling matrix Z_{21}. Indeed, the matrix-vector product with Z_{12} is not reduced with the hybridization but the matrix-vector product with Z_{21} (rough surface toward the object) is divided by 2 due to PO shadowing (see Fig. 3): the mean of the two complexities implies $T_{12} = 3N_1N_2/4$.

From Table I, the hybrid method has a lower theoretical complexity in terms of computing time.

Comparison of computing time (closely related to the complexity) of the hybrid and rigorous methods is plotted in Fig. 12 versus the number of unknowns on the plate; a plate above a rough surface is considered. Same parameters as in Fig. 7 are considered but the plate length is not a constant.

Comparison of computing time of the hybrid and rigorous methods is plotted in Fig. 13 versus the number of unknowns on the cross; a cross above a rough surface is considered. Same parameters as in Fig. 9 are considered but with TM polarization and the cross size is not a constant.

As expected, from Figs. 12 and 13, the hybrid method permits us to reduce considerably the computing time. The complexity

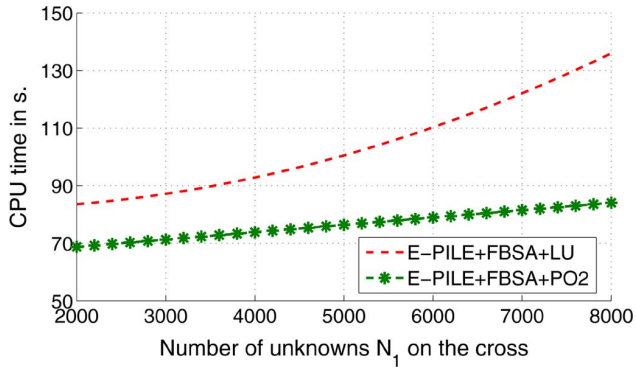

Fig. 13. Comparison of computing time of the hybrid and rigorous methods versus the number of unknowns on the object for a cross above a rough surface. Same parameters as in Fig. 9 but with TM polarization.

TABLE II
STORAGE REQUIREMENTS (NUMBER OF COMPLEX ELEMENTS) E-PILE+FBSA, E-PILE+FBSA+PO1 (PLATE CASE) AND E-PILE+FBSA+PO2 (CROSS CASE) FOR EACH IMPEDANCE MATRIX INVOLVED IN THE E-PILE PROCESS

Configuration \ Impedance matrix	$\bar{\boldsymbol{Z}}_1$	$\bar{\boldsymbol{Z}}_{12}$	$\bar{\boldsymbol{Z}}_{21}$	$\bar{\boldsymbol{Z}}_2$
E-PILE+FBSA	N_1^2	N_1N_2	N_1N_2	$\approx N_2N_s$
E-PILE+FBSA+PO1	1	N_1N_2	$\frac{N_1N_2}{2}$	$\approx N_2N_s$
E-PILE+FBSA+PO2	$\frac{N_1^2}{8}$	N_1N_2	$\frac{N_1N_2}{2}$	$\approx N_2N_s$

increases as N_1 increases for the hybrid method with the cross case since the DR are taken into account ($T_{11} = N_1^2/8$ since only $1/8$ of the $\bar{\boldsymbol{C}}_{\mathbf{DR}}$ matrix are non-zero elements as illustrated in Fig. 5) whereas for the plate case the complexity does not depend on $N_1 (T_{11} = 1)$.

C. Memory Requirements

One can evaluate the theoretical storage requirements by considering the plate and the cross above a rough surface for three methods: the MoM (with direct LU inversion of the impedance matrix of the whole scene), the E-PILE+FBSA (with direct LU inversion on the object) and E-PILE+FBSA+PO. The MoM needs to store $(N_1 + N_2)^2$ complex elements. The memory requirements for each matrix involved in the E-PILE process are listed in Table II for E-PILE+FBSA, E-PILE+FBSA+PO1 and E-PILE+FBSA+PO2.

Comparison of theoretical storage requirements of the classical MoM (LU inversion for the scene), the rigorous fast method E-PILE+FBSA+LU (LU inversion only on the object) and the hybrid E-PILE+FBSA+PO method are plotted in Fig. 14 versus the number of unknowns on the plate; a plate above a rough surface is considered. Same parameters as in Fig. 12 are considered. Comparison of theoretical storage requirements of the classical MoM (LU inversion for the scene), the rigorous fast method E-PILE+FBSA+LU (LU inversion only on the object) and the hybrid E-PILE+FBSA+PO method are plotted in Fig. 15 versus the number of unknowns on the cross; a cross above a rough surface is considered. Same parameters as in Fig. 13 are considered.

From Figs. 14 and 15, one can see that the E-PILE method combined with the FBSA permits us to significantly reduce

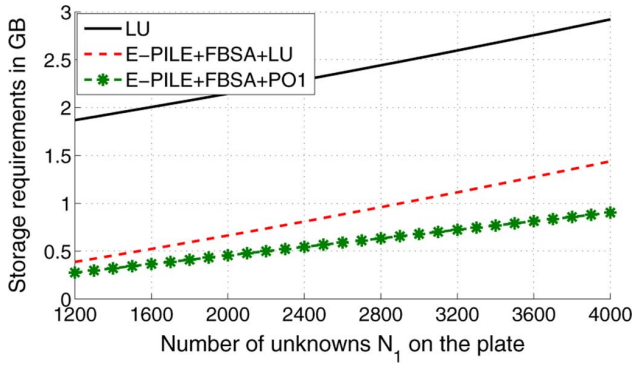

Fig. 14. Theoretical storage requirements in Gigabytes for the plate above a rough surface versus the number of unknowns N_1 on the plate. Three methods are considered : the classical MoM, the E-PILE+FBSA+LU method and the E-PILE+FBSA+PO method.

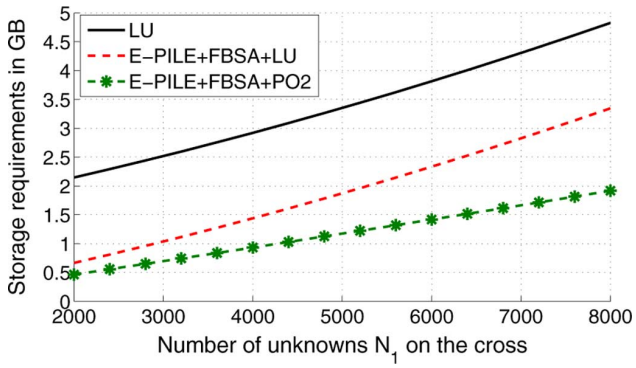

Fig. 15. Theoretical storage requirements in Gigabytes for the cross above a rough surface versus the number of unknowns N_1 on the cross. Three methods are considered : the classical MoM, the E-PILE+FBSA+LU method and the E-PILE+FBSA+PO method.

the storage requirements. Nevertheless, the direct LU inversion on the object cannot be done in a standard computer for large number of unknowns on the object N_1. For example, by using a computer with 2 GB of RAM, the theoretical limit for E-PILE+FBSA+LU is $N_1 \approx 5000$ for a cross above a rough surface (see Fig. 15) with $N_2 = 10000$ whereas, using the hybrid method pushes this limit to $N_1 \approx 8000$. Thus, if a very large object (with dihedral effects) above a very long rough surface is considered, the hybrid method permits us to obtain some quite accurate results with a low computing time by using a standard personal computer when rigorous method cannot be applied. The main cost in terms of both computing time and storage requirements in the E-PILE process remains the coupling step. Further works in the same way as in [20] for scattering from a rough layer, could provide a solution to reduce the coupling step complexity.

IV. Conclusion

In this paper, a new hybrid numerical method for the scattering from an electrically large perfectly-conducting object with dihedral effects above a very long one-dimensional rough surface is proposed. The extended-PILE method is combined with the forward-backward spectral acceleration (FBSA) for the local interactions on the rough surface and with the second-order physical optics (PO2) approximation for the local interactions on the object. First, the case of the plate above a rough surface is studied and the first-order PO is applied in the E-PILE iterative scheme. Then, by considering a cross above a rough surface, E-PILE+FBSA is combined with the second-order PO. By assuming a Gaussian process with a Gaussian height spectrum, this new hybrid method, E-PILE+FBSA+PO2, is tested against the rigorous E-PILE+FBSA method as functions of the object inclination, the polarization and the incidence angle. These results have shown that the hybrid method provides a good accuracy on the RCS except for grazing observation angles. This new hybrid method is particularly interesting for problems that imply a very high number of unknowns that can be solved neither by the MoM with a direct LU inversion nor by the rigorous fast E-PILE+FBSA method. Indeed, the study of the complexity has shown that both CPU time and storage requirements are considerably reduced with E-PILE+FBSA+PO2.

Appendix A
Computation of the Coupling Matrix $\bar{\boldsymbol{Z}}'_{\boldsymbol{21}}$ for TE Polarization

For the general case of a dielectric rough surface, the coupling matrix $\bar{\boldsymbol{Z}}_{\boldsymbol{21}}$ propagates the total surface field ψ_2 and its normal derivative $\partial\psi_2/\partial n_2$ (at the point $\boldsymbol{r}_{\boldsymbol{2_n}} \in S_2$) toward the object (at the point $\boldsymbol{r}_{\boldsymbol{1_m}} \in S_1$).

A. Propagation of $\partial\psi_2/\partial n_2$

For the propagation of $\partial\psi_2/\partial n_2, (\bar{\boldsymbol{Z}}_{\boldsymbol{21}})_{mn}$ is obtained by sampling the Green function (first part of the integrand of the Huygens principle)

$$(\bar{\boldsymbol{Z}}_{\boldsymbol{21}})_{mn} = g_0(\boldsymbol{r}_{\boldsymbol{2}}, \boldsymbol{r}_{\boldsymbol{1}})\,\mathrm{d}s_2\,|_{r_2=r_{2_n};r_1=r_{1_m}} \tag{28}$$

with

$$g_0(\boldsymbol{r}_{\boldsymbol{2}}, \boldsymbol{r}_{\boldsymbol{1}})\,\mathrm{d}s_2 = af(u(x_1, z_1, x_2, z_2)) \tag{29}$$

in which

$$\begin{cases} a = \dfrac{i\sqrt{1+(\gamma_2)^2}\,\mathrm{d}x_2}{4} \\ f(u) = H_0^{(1)}(u), \\ u(x_1, z_1, x_2, z_2) = k_0 r = u \\ r = \sqrt{(x_{12})^2 + (z_{12})^2} \\ x_{12} = x_1 - x_2 \\ z_{12} = z_1 - z_2. \end{cases} \tag{30}$$

Since

$$(\bar{\boldsymbol{Z}}'_{\boldsymbol{21}})_{mn} = \frac{\partial \bullet}{\partial n_1}(\bar{\boldsymbol{Z}}_{\boldsymbol{21}})_{mn}(\beta_{21})_{mn} \tag{31}$$

and from (28) and (29), we have

$$(\bar{\boldsymbol{Z}}'_{\boldsymbol{21}})_{mn} = a\frac{\partial f(u)}{\partial n_1}\bigg|_{r_2=r_{2_n};r_1=r_{1_m}} (\beta_{21})_{mn} \tag{32}$$

in which, the first part in right-hand side is given (before sampling) by

$$a\frac{\partial f(u)}{\partial n_1} = a\frac{v}{\sqrt{1+\gamma_1^2}}\left(-\gamma_1\frac{\partial f(u)}{\partial x_1} + \frac{\partial f(u)}{\partial z_1}\right) \tag{33}$$

with

$$\frac{\partial f(u)}{\partial x_1} = -k_0 H_1^{(1)}(u)\frac{x_{12}}{r} \tag{34}$$

$$\frac{\partial f(u)}{\partial z_1} = -k_0 H_1^{(1)}(u)\frac{z_{12}}{r}. \tag{35}$$

The continuous variables $x_1, z_1, x_2, z_2, v, \gamma_1, \gamma_2, \mathrm{d}x_2$ are replaced, in (33), (34), (35) and (30), by the discrete variables $x_{1_m}, z_{1_m}, x_{2_n}, z_{2_n}, v_m, \gamma_{1_m}, \gamma_{2_n}, \Delta x_{2_n}$, respectively, to obtain (32).

B. Propagation of ψ_2

For the propagation of ψ_2, $(\bar{\boldsymbol{Z}}_{\boldsymbol{21}})_{mn}$ is obtained by sampling the normal derivative of the Green function (second part of the integrand of the Huygens principle)

$$(\bar{\boldsymbol{Z}}_{\boldsymbol{21}})_{mn} = \left.\frac{\partial g_0(\boldsymbol{r_2}, \boldsymbol{r_1})}{\partial n_2}\,\mathrm{d}s_2\right|_{r_2=r_{2_n};r_1=r_{1_m}} \tag{36}$$

with

$$\frac{\partial g_0(\boldsymbol{r_2}, \boldsymbol{r_1})}{\partial n_2}\,\mathrm{d}s_2 = \frac{a}{\sqrt{1+\gamma_2^2}}\left(-\gamma_2\frac{\partial f(u)}{\partial x_2} + \frac{\partial f(u)}{\partial z_2}\right) \tag{37}$$

in which

$$\frac{\partial f(u)}{\partial x_2} = k_0 H_1^{(1)}(u)\frac{x_{12}}{r} \tag{38}$$

$$\frac{\partial f(u)}{\partial z_2} = k_0 H_1^{(1)}(u)\frac{z_{12}}{r}. \tag{39}$$

Since

$$(\bar{\boldsymbol{Z}}'_{\boldsymbol{21}})_{mn} = \frac{\partial^\bullet}{\partial n_1}(\bar{\boldsymbol{Z}}_{\boldsymbol{21}})_{mn}(\beta_{21})_{mn} \tag{40}$$

and from (36) and (37), we have

$$(\bar{\boldsymbol{Z}}'_{\boldsymbol{21}})_{mn} = \left.\frac{\partial^2 g_0(\boldsymbol{r_2}, \boldsymbol{r_1})}{\partial n_1 \partial n_2}\,\mathrm{d}s_2\right|_{r_2=r_{2_n};r_1=r_{1_m}} (\beta_{21})_{mn} \tag{41}$$

in which the first part in right-hand side is given (before sampling) by

$$\frac{\partial^2 g_0(\boldsymbol{r_2}, \boldsymbol{r_1})}{\partial n_1 \partial n_2}\,\mathrm{d}s_2 = \frac{v}{\sqrt{1+\gamma_1^2}}\left(-\gamma_1\frac{\partial^2 g_0(\boldsymbol{r_2}, \boldsymbol{r_1})}{\partial x_1 \partial n_2}\,\mathrm{d}s_2 + \frac{\partial^2 g_0(\boldsymbol{r_2}, \boldsymbol{r_1})}{\partial z_1 \partial n_2}\,\mathrm{d}s_2\right) \tag{42}$$

and, from (30), we have

$$\frac{\partial^2 g_0(\boldsymbol{r_2}, \boldsymbol{r_1})}{\partial n_1 \partial n_2}\,\mathrm{d}s_2 = \frac{iv\,\mathrm{d}x_2}{4\sqrt{1+\gamma_1^2}}\left(\gamma_1\gamma_2\frac{\partial^2 f(u)}{\partial x_1 \partial x_2} - \gamma_1\frac{\partial^2 f(u)}{\partial x_1 \partial z_2} - \gamma_2\frac{\partial^2 f(u)}{\partial z_1 \partial x_2} + \frac{\partial^2 f(u)}{\partial z_1 \partial z_2}\right) \tag{43}$$

with

$$\frac{\partial^2 f(u)}{\partial x_1 \partial x_2} = \frac{x_{12}^2 k_0^2 h_{10}(u)}{r^2} - \frac{k_0\left(x_{12}^2 - z_{12}^2\right)h_{11}(u)}{r^3} \tag{44}$$

$$\frac{\partial^2 f(u)}{\partial x_1 \partial z_2} = x_{12} z_{12} k_0\left(\frac{k_0 h_{10}(u)}{r^2} - \frac{2h_{11}(u)}{r^3}\right) \tag{45}$$

$$\frac{\partial^2 f(u)}{\partial z_1 \partial x_2} = x_{12} z_{12} k_0\left(\frac{k_0 h_{10}(u)}{r^2} - \frac{2h_{11}(u)}{r^3}\right) \tag{46}$$

$$\frac{\partial^2 f(u)}{\partial z_1 \partial z_2} = \frac{z_{12}^2 k_0^2 h_{10}(u)}{r^2} + \frac{k_0\left(x_{12}^2 - z_{12}^2\right)h_{11}(u)}{r^3} \tag{47}$$

in which

$$h_{10}(u) = H_0^{(1)}(k_0 r) = f(u) \tag{48}$$

$$h_{11}(u) = H_1^{(1)}(k_0 r). \tag{49}$$

The continuous variables $x_1, z_1, x_2, z_2, v, \gamma_1, \gamma_2, \mathrm{d}x_2$ are substituted, in (43)–(49), (35) and (30), for the discrete variables $x_{1_m}, z_{1_m}, x_{2_n}, z_{2_n}, v_m, \gamma_{1_m}, \gamma_{2_n}, \Delta x_{2_n}$, respectively, to obtain (41).

APPENDIX B
COMPUTATION OF THE COUPLING MATRIX $\bar{\boldsymbol{C}}_{\mathbf{DR}}$ FOR THE DR OF THE CROSS

For a PC cross, the coupling matrix $\bar{\boldsymbol{C}}_{\mathbf{DR}}$ propagates the total surface field ψ_1 (for TM polarization) or its normal derivative $\partial\psi_1/\partial n_1$ (for TE polarization) from the face f_i (at the point $\boldsymbol{r}_{\mathbf{1_n}} \in S_{f_i}$) toward the opposite face f_j (at the point $\boldsymbol{r}_{\mathbf{1_m}} \in S_{f_j}$). f_i stands for the ith face and f_j the jth face of the cross.

A. Propagation of ψ_1: TM Polarization

For the propagation of ψ_1, $(\bar{\boldsymbol{C}}_{\mathbf{DR}})_{mn}$ is obtained by sampling the normal derivative of the Green function (first part of the integrand of the Huygens principle)

$$(\bar{\boldsymbol{C}}_{\mathbf{DR}})_{mn} = \left.\frac{\partial g_0(\boldsymbol{r}_{\mathbf{1}_{f_i}}, \boldsymbol{r}_{\mathbf{1}_{f_j}})}{\partial n_{1_{f_i}}}\,\mathrm{d}s_{1_{f_i}}\right|_{r_{1_{f_i}}=r_{1_n};r_{1_{f_j}}=r_{1_m}} \tag{50}$$

in which n is the index of an element of face f_i and m the index of an element of face f_j of the cross. This equation is similar to (36), thus, $(\bar{\boldsymbol{C}}_{\mathbf{DR}})_{mn}$ is given from (50) by using (37), (38) and (39) in which the subscripts 2 and 1 are substituted for the subscripts 1_{f_i} and 1_{f_j}, respectively. In contrary to the rough surface, $\hat{\boldsymbol{n}}_{\mathbf{1}_{\boldsymbol{f_i}}}$ can be oriented in $-\hat{\boldsymbol{z}}$ direction and $\mathrm{d}x_{1_{f_i}}$ can be

negative, this implies to multiply (37) by the orientation of the normal vector of the face f_i: $v_{1_{f_i}}$ and to take the absolute value of $\mathrm{d}x_{1_{f_i}}$ to insure a positive surface element.

B. Propagation of $\partial\psi_1/\partial n_1$: TE Polarization

For TE polarization, the PO2 approximation implies to propagate $\partial\psi_1/\partial n_1$ from the face f_i toward the opposite face f_j in order to obtain $\partial\psi_1/\partial n_1$ on the face f_j, which means a second normal derivative operating on the Green function

$$(\bar{\boldsymbol{C}}_{\mathbf{DR}})_{mn} = \left.\frac{\partial^2 g_0(\boldsymbol{r}_{\mathbf{1}_{\boldsymbol{f_i}}}, \boldsymbol{r}_{\mathbf{1}_{\boldsymbol{f_j}}})}{\partial n_{1_{f_j}} \partial n_{1_{f_i}}} \mathrm{d}s_{1_{f_i}}\right|_{r_{1_{f_i}}=r_{1_n}; r_{1_{f_j}}=r_{1_m}} \tag{51}$$

which is similar to (41). Thus, once again, the detailed calculus of Appendix A can be used by subscript substitutions and by taking care of normal directions and positive surface elements on the object.

REFERENCES

[1] J. T. Johnson and R. J. Burkholder, "Coupled canonical grid/discrete dipole approach for computing scattering from objects above or below a rough interface," *IEEE Trans. Geosci. Remote Sensing*, vol. 39, no. 6, pp. 1214–1220, Jun. 2001.

[2] J. T. Johnson, "A numerical study of scattering from an object above a rough surface," *IEEE Trans. Antennas Propag.*, vol. 50, no. 10, pp. 1361–1367, 2002.

[3] J. T. Johnson, "A study of the four-path model for scattering from an object above a half space," *Microw. Opt. Tech. Lett.*, vol. 30, no. 2, pp. 130–134, Jul. 2001.

[4] T. Chiu and K. Sarabandi, "Electromagnetic scattering interaction between a dielectric cylinder and a slightly rough surface," *IEEE Trans. Antennas Propag.*, vol. 47, no. 5, pp. 902–913, May 1999.

[5] Y. Zhang, Y. E. Yang, H. Braunisch, and J. A. Kong, "Electromagnetic wave interaction of conducting object with rough surface by hybrid SPM/MoM technique," *Progr. Electromagn. Res.*, vol. 22, pp. 315–335, 1999.

[6] X. Wang, C.-F. Wang, Y.-B. Gan, and L.-W. Li, "Electromagnetic scattering from a circular target above or below rough surface," *Progr. Electromagn. Res.*, vol. 40, pp. 207–227, 2003.

[7] L.-X. Guo, A.-Q. Wang, and J. Ma, "Study on EM scattering from 2D target above 1-D large scale rough surface with low grazing incidence by parallel MoM based on PC clusters," *Progr. Electromagn. Res.*, vol. 89, pp. 149–166, 2009.

[8] P. Liu and Y. Q. Jin, "The finite-element method with domain decomposition for electromagnetic bistatic scattering from the comprehensive model of a ship on and a target above a large scale rough sea surface," *IEEE Trans. Geosci. Remote Sensing*, vol. 42, no. 5, pp. 950–956, May 2004.

[9] G. Kubické, C. Bourlier, and J. Saillard, "Scattering by an object above a randomly rough surface from a fast numerical method: Extended PILE method combined with FB-SA," *Waves Random Complex Media*, vol. 18, no. 3, pp. 495–519, Aug. 2008.

[10] G. Kubické, C. Bourlier, and J. Saillard, "Scattering from canonical objects above a sea-like one-dimensional rough surface from a rigorous fast method," *Waves Random Complex Media*, vol. 20, no. 1, pp. 156–178, Feb. 2010.

[11] N. Déchamps, N. De Beaucoudrey, C. Bourlier, and S. Toutain, "Fast numerical method for electromagnetic scattering by rough layered interfaces: Propagation-inside-layer expansion method," *J. Opt. Society Amer. A.*, no. 23, pp. 359–369, 2006.

[12] H. T. Chou and J. T. Johnson, "A novel acceleration algorithm for the computation of scattering from rough surfaces with the forward-backward method," *Radio Sci.*, vol. 33, pp. 1277–1287, 1998.

[13] M. R. Pino, F. Obelleiro, L. Landesa, and R. J. Burkholder, "Application of the fast multipole method to the generalized forward-backward iterative algorithm," *Microw. Opt. Tech. Lett.*, vol. 26, no. 2, pp. 78–83, July 2000.

[14] H. Ye and Y.-Q. Jin, "Fast iterative approach to difference electromagnetic scattering from the target above a rough surface," *IEEE Trans. Geosci. Remote Sensing*, vol. 44, no. 1, pp. 108–115, Jan. 2006.

[15] H. Ye and Y.-Q. Jin, "A hybrid analytic-numerical algorithm of scattering from an object above a rough surface," *IEEE Trans. Geosci. Remote Sensing*, vol. 45, no. 5, pp. 1174–1180, 2007.

[16] G. Kubické, C. Bourlier, and J. Saillard, "A new hybrid numerical method for the scattering by a plate above a rough surface," presented at the 26th Progr. Electromagn. Res. Symp. (PIERS), Moscow, Russia, Aug. 18–21, 2009.

[17] E. I. Thorsos, "The validity of the Kirchhoff approximation for rough surface scattering using a Gaussian roughness spectrum," *J. Acoust. Society Amer.*, no. 83, pp. 78–92, 1988.

[18] L. Tsang, J. A. Kong, K.-H. Ding, and C. O. Ao, *Scattering of Electromagnetic Waves: Volume II. Numerical Simulations*, ser. Series on Remote Sensing. New York: Wiley, 2001.

[19] C. Bourlier, G. Kubické, and N. Déchamps, "A fast method to compute scattering by a buried object under a randomly rough surface: PILE combined with FB-SA," *J. Opt. Society Amer. A.*, vol. 25, no. 4, pp. 891–902, Apr. 2008.

[20] N. Déchamps and C. Bourlier, "Electromagnetic scattering from a rough layer: Propagation-inside-layer expansion method combined to an updated BMIA/CAG approach," *IEEE Trans. Antennas Propag.*, vol. 55, no. 10, pp. 2790–2802, 2007.

Gildas Kubické was born in Longjumeau, France, in September 1982. He received the Engineering degree and M.S. degree in electronics and electrical engineering both in 2005 and the Ph.D. degree in 2008 from the University of Nantes, France.

He is currently a Research Engineer in the SEC Team of IREENA Laboratory (Institut de Recherche en Electrotechnique et Electronique de Nantes Atlantique, France) at Polytech'Nantes (University of Nantes, France). His research interest includes electromagnetic scattering and radar cross section modeling.

Christophe Bourlier (M'99) was born in La Flèche, France, on July 6, 1971. He received the M.S. degree in electronics from the University of Rennes, France, in 1995 and the Ph.D. degree from the Polytech'Nantes (University of Nantes, France), in 1999.

While at the University of Rennes, he was with the Laboratory of Radiocommunication where he worked on antennas coupling in the VHF-HF band. Currently, he is with the IREENA Laboratory (Institut de Recherche en Electrotechnique et Electronique de Nantes Atlantique, France) in the SEC team at Polytech'Nantes (University of Nantes, France). He works as an Assistant Researcher of National Center for Scientific Research on electromagnetic wave scattering from rough surfaces and objects for remote sensing applications. He is author of more than 120 journal articles and conference papers.